Cellulose Nanocrystals in Spherical Titania-Sol Microdroplet: From Dynamic Self-Assembly to Nanostructured TiO x /C Microsphere Synthesis

Cong Wang, Erwan Paineau, Hynd Remita, Mohamed Nawfal Ghazzal

Cellulose Nanocrystals in Spherical Titania-Sol Microdroplet: From Dynamic Self-Assembly to Nanostructured TiOx/C Microsphere Synthesis

Wang, C.; Paineau, E. ; Remita, H. ; Ghazzal, M. N. Chem. Mater. 33, 17, 6925–6933 (2021)doi.org/10.1021/acs.chemmater.1c01865

5.1 Introduction

Cellulose nanocrystals (CNCs) are spindle-like rods derived from a variety of natural resources via strong acid hydrolysis,[1] which can spontaneously organize into a cholesteric structure, called chiral nematic (CN) structure.[2-4] The self-organization of CNCs into well-ordered CN liquid crystals are ubiquitous in nature,[5] inspiring widespread interest in the development of green functional materials with versatile applications, such as biomimetic nanomaterials, soft nanotechnology, optoelectronics and photocatalysis technology.[6-9]

The transfer of such natural CN nanostructures into artificial spherical functional materials on the nano- or micro-scale, however, is challenging.[10] Typically, studies have focused on obtaining long-range ordered CN structure in planar functional films by using evaporation-induced self-assembly (EISA) method.[11-14] To obtain this CN structure in a small film area, i.e. microfilms, EISA is not applicable and the use of a sophisticated printing method is required.[15] Evaporation is essential to achieve equilibrium during isotropic-to-anisotropic transition. The phase transition starts with the nucleation of helical twist in localized spaces, which are called tactoids. As a key component for fundamentally understanding of the self-assembly process of CN structure, tactoids can dynamically bridge the disordered isotropic phase and the ordered CN phase.[16] The importance of tactoids in constructing functional material by controlling the liquid crystal properties has been highlighted, since Lagerwall and coworkers showed that the optical properties of the photonic films could be improved by applying shear forces to suspensions of CNCs during drying.[17] The shear forces improved the alignment of the tactoids, and consequently ameliorated the quality of the films. In planar geometries, water evaporation of the CNCs suspension will initiate the coalescence and sedimentation of tactoids, and eventually compress them into long-range lamellar liquid crystalline phase.[18] Significantly, such planar organization mechanism is not applicable to three-dimensional constrained geometry, especially to target materials with spherical morphology that exceed the restriction of film shape.

Spherical confinement of CN liquid crystals are of particular interest in potential applications of sensing, actuators or lasers, optical devices and chiral molecular switches, due to their triggered novel topological structures and special geometries.[19-24] However, only a few attempts have been dedicated to investigate the CN structure of CNCs aqueous suspension in confined microdroplets.[25-29] Although these studies have macroscopically described the evolution of CNCs under spherical constraint as a simple isotropic-to-anisotropic phase transition, the exhaustive organization process remains largely unexplored, in particular with regard to the involvement of inorganic precursors. Moreover, the stability of precursors (metal chlorides or alkoxides) is highly sensitive to moisture, leading to a fast condensation which destabilizes the CN structure into the isotropic phase.[7] Thus, further investigations aimed at providing additional insights in the organization process of CNCs in water or in the presence of precursors are meaningful and necessary.

5.2 Objectives

The study and control of CNCs self-assembly in spherical confinement remains a challenging and unexplored area. It is difficult to directly observe the self-organization of CNCs in such geometry. In this chapter, we reported a dynamic observation of the self-organization process of CNCs in confined titania-sol microdroplet. The isotropic to cholesteric transition undergoes nucleation, coalescence and migration of tactoids through two coalescence mechanisms, namely "head-to-tail" and "side-to-side" types. The solubility and self-organization of CNCs in titania-sol enable a successful transfer of the chiral nematic structure into hybrid TiO_x/C microspheres. TiO_x/C microspheres show higher photocatalytic H_2 generation compared to TiO_2-P25. This chapter adds to the understanding of self-assembly process of CNCs in spherical geometry.

5.3 Preparation of microdroplets and microspheres

5.3.1 Materials

All solvents and reagents including Span 80 (viscosity 1000-2000 mPa.s, 20 °C), cyclohexane (99.7%), TAA (Titanium diisopropoxide bis(acetylacetonate), 75 wt.% in isopropanol), TiO_2-P25 (80% anatase, 20% rutile) and CNCs (Cellulose Nanocrystals, obtained from University of MAINE) were used without further purification.

5.3.2 Preparation of TAA/CNC mixtures

Different volumes of TAA solutions (**Table S5-1**) were added in 1 mL ethanol stirred for 10 min, then mixed with 5 mL CNCs aqueous suspension (pH = 6.3). Homogeneous transparent yellow mixtures can be obtained after 30 min stirring under room temperature.

5.3.3 Fabrication of TAA/CNC microdroplets and TiO_x/C microspheres

Typically, Span 80 (0.47g) was mixed with cyclohexane (30 mL) and sonicated for 10 min to obtain a transparent solution, then transferred to a 100 mL round-bottom flask with magnetic stir bar. The prepared TAA/CNC solution was added dropwise into the flask and maintained a stirring speed at 500 rpm. After rapid-term emulsification at ambient temperature (20 °C), allowing the original state to be studied under POM. The effect of temperature on the CN structure was investigated by changing the emulsification temperature (varied from 20 to 100 °C). To synthesize the TiO_x/C microspheres, TAA/$CNC_{6\%}$ microdroplets were emulsified in a sealed flask at 60 °C for 90 min, then introduced into a Teflon-lined autoclave (50 mL) and heated at 180 °C for 18 h. The black solid microspheres were washed with ethanol and collected by centrifugation, then dried overnight in oven.

5.4 Optimization of CNCs concentration

To understand the role of spherical confinement, it is necessary to investigate first the influence of initial CNCs concentration before encapsulation. The main objective is the optimization of CNCs content in titania-sol, ensuring the spontaneous phase transition from isotropic to chiral nematic. This phase transition depends on the concentration of CNCs, but also on the pH, ionic salt and residual sulfur ratio.[30-32] Considering these facts, variable concentrations of CNCs suspension blended with different volumes of $Ti(acac)_2(OiPr)_2$ (TAA) precursor under constant pH (~ 6) were prepared (**Figure 5-1c, Figure S5-1 and Table S5-1**), where acetylacetonate is used as a chelating agent to inhibit fast condensation of the precursor.[7] The CNCs suspensions exhibited birefringence under polarized light (**Figure 5-1a**). Typical fingerprint-like structures with alternated bright and dark lines can also be observed under POM, which indicated the formation of CN phases (**Figure 5-1b and Figure S5-2**).[3] The addition of TAA precursor led to the dilution of CNCs suspensions, resulting in the reversion from CN phase to isotropic phases (shown black domain under POM) (**Figure 5-1d**).[33-35]

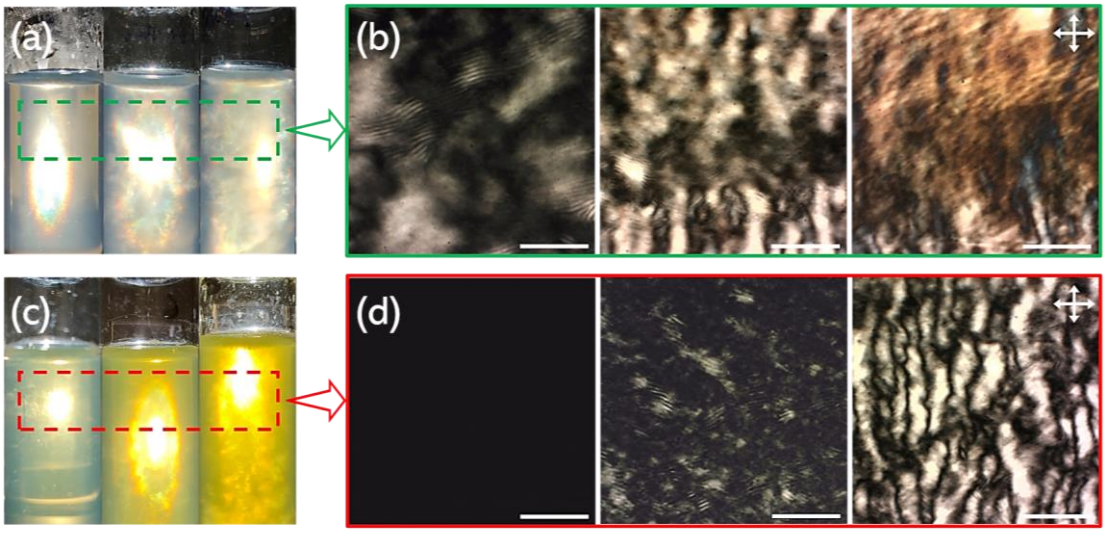

Figure 5-1. (a) Photographs under polarized light and (b) typical POM images of CNCs suspensions (from left to right, $CNC_{4\%}$, $CNC_{6\%}$, and $CNC_{8\%}$). (c) Photographs under polarized light and (d) POM images of TAA/CNC mixtures (from left to right, $TAA/CNC_{4\%}$, $TAA/CNC_{6\%}$, and $TAA/CNC_{8\%}$). All scale bars correspond to 50 μm.

The birefringence and fingerprint patterns reappeared when the CNCs concentration further increased. The distances between bright and dark lines correspond to half of the helical pitch (*P*, defined as the distance for a 360° rotation of CNCs rod), which is the key characteristic of CN phase.[36, 37] The value of *P* tightened from 6.2 to 3.2 μm as the concentration increased from 4 to 6 wt %, which has been attributed to the close packing of the CNCs rods, thus resulting in stronger intermolecular interactions as well as more pronounced birefringence (**Figure 5-1a, Figure 5-2 and Table S5-2**).[38, 39]

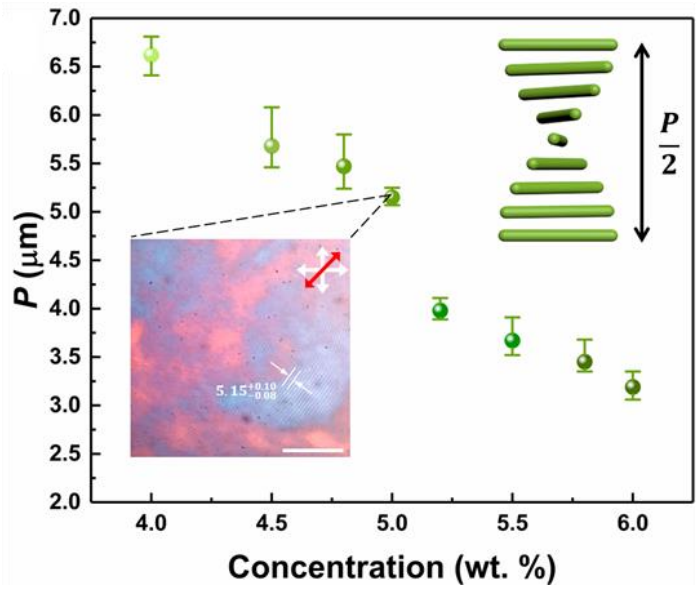

Figure 5-2. Variation of the helical pitch value with the CNCs mass fraction. The insets include a schematic representation of half pitch (*P*/2) and a representative POM image of $CNC_{5\%}$ (showing a *P* value of 5.15 μm) recorded with a retardation λ-plate (530 nm). Scale bar = 50 μm

In this concentration range, the magnitude of the *P* should scale with the inverse of the aspect ratio, $P \propto D/L$, which is usually observed for colloidal solution.[37, 40] In our case, the *P* is inversely proportional to concentration, $P \propto C^{-1}$, and the fraction of the anisotropic phase to the isotropic phase, as expected from Straley modelling of chiral nonflexible rods.[41] Moreover, two main mechanisms could be involved in rationalizing the decrease in *P* as the CNCs concentration increased.[42] The first one is related to the helix formation. Basically, the chirality transfer in liquid crystals is driven by the

transfer of the chirality of the molecular cellulose to the macroscopic ordering of the liquid crystal phase. The larger the amount of CNCs in the solution, the stronger the total cohesion of the twist.[43] The second one is driven by the increase of the ionic strength (due to the negatively charged CNCs rods) upon increasing the CNCs concentration. This leads to an exponential decay of the electrostatic repulsion and thus allows CNCs rods closer to each other. Notably, the value of *P* tended to level off at high concentrations (> 6 wt%), accompanied by obvious birefringence (**Figure 5-3**).[44]

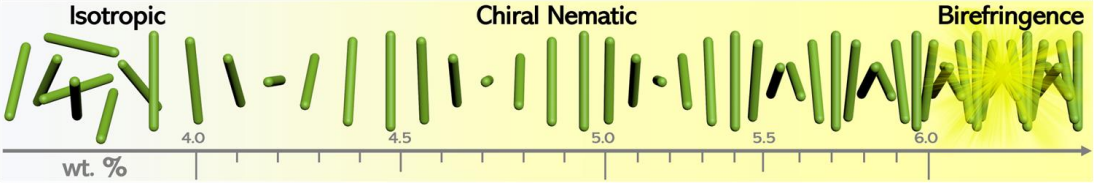

Figure 5-3. Schematics of chiral nematic structure (from isotropic phase to chiral nematic phase and obvious birefringence).

5.5 Production of TAA/CNC microdroplets

With these results, inverse microemulsion method was employed to encapsulate CNCs and TAA/CNC microdroplets with diameter (Φ) of 110 ~ 170 μm (**Figure 5-4a and Table S5-3**). Compared with microfluidic, the size distribution of micodroplets through microemulsion method is less well controlled. However, this simple method enables the rapid emulsification of microdroplets and is easy to implement, offering the opportunity to capture and investigate the primitive states of tactoids by using POM. The use of water-in-oil microemulsion avoids the evaporation of water from the microdroplets, allowing the self-organization in confined microspheres to be studied over time scales from seconds to hours. In standard procedure, 3 mL of the sonicated CNCs suspensions or TAA/CNC mixtures were added dropwise into cyclohexane (30 mL, containing 2 wt% Span 80) under constant stirring speed (500 rpm) to obtain relatively uniform microdroplets. Fresh microdroplets were collected into an unsealed capillary after 1 min emulsification at ambient temperature (20 °C), allowing the

primitive state to be studied under POM. The concentration of CNCs suspensions varied from 4 to 8 wt%, in order to assess the threshold at which the isotropic-to-anisotropic phase transition occurred in microdroplets. The optical characteristics of CNCs in microdroplets are similar to that observed in homogeneous suspensions (**Figure 5-4b-g and Figure S5-3**). However, for newly collected microdroplets, especially at low CNCs ratio, the isotropic phase was predominant.

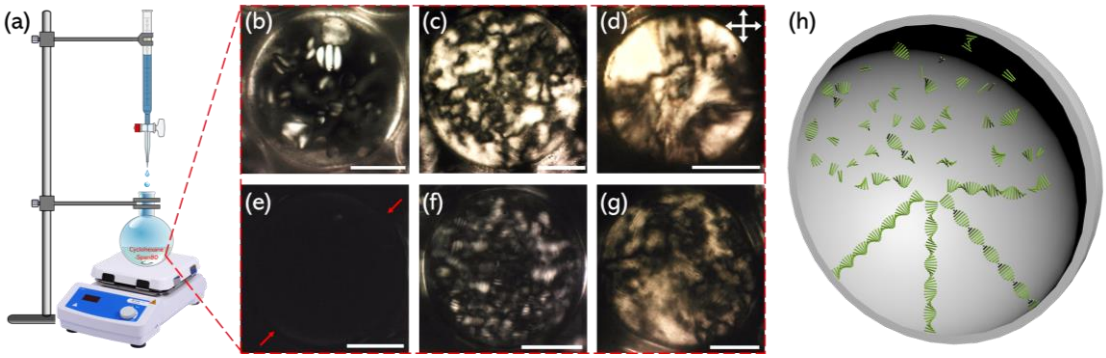

Figure 5-4. (a) Cartoon illustration of inverse microemulsion system. POM images of microdroplets of (b) $CNC_{4\%}$, (c) $CNC_{6\%}$, (d) $CNC_{8\%}$, (e) $TAA/CNC_{4\%}$, (f) $TAA/CNC_{6\%}$ and (g) $TAA/CNC_{8\%}$ (scale bars = 50 μm). (h) Schematic of microdroplet.

CNCs rods start to self-organize in birefringent tactoids that nucleate and grow over time (**Figure 5-4 b, f**). Onsager, in his pioneering work,[45] predicted that homogeneous dispersions of rod particles with high aspect ratios may undergo a phase separation spontaneously. This is due to a competition between orientational entropy and free volume entropy due to excluded-volume interactions. Intuitive observation of POM showed that the dark areas were gradually replaced by bright bands, indicating the onset of isotropic to CN phase transition (nucleation of tactoids). At this primitive nonequilibrium state, the value of *P* in tactoids is generally higher than that in suspensions (**Table S5-1 and S5-3**). In addition, the *P* value for TAA/CNC microdroplets is further expanded compared to CNCs microdroplets, owing to the insertion of the TAA precursor. Tactoid formation progressed weakly (may last several hours) under a low concentration of CNCs. The low local density reduces the probability of interactions between the CNCs rods, which slows down their interactions

and phase transition kinetics. Comparatively, nucleation and coalescence can proceed simultaneously at higher concentrations (**Figure 5-4 f, h**). Based on these findings, we focus on following the case of TAA/$CNC_{6\%}$ microdroplet to ensure the acquisition of detailed information on the nucleation and coalescence mechanism of tactoids in confined titania-sol microdroplet for a short period.

5.6 Revealing the evolution process

To further investigate the evolution process from isotropic to Ch nematic phase and reveal the growth mechanism of tactoids in spherical confinement, the internal structure progress of one TAA/$CNC_{6\%}$ microdroplet (Φ ~ 110 μm) was tracked under POM after ~30 seconds of rapid-term emulsification at 20 °C (**Figure 5-4**). The use of a lambda retardation plate allowed us to determine the preferred orientation of CNCs directors in the CN phase within the microdroplet (**Figure 5-4 b1-b8**). At the beginning, isotropic phases dominated the microdroplet, in which small tactoids started to nucleate with one or two periodic bands (**Figure 5-4 a1-c1**). After 60 seconds of evolution, newborn tactoids grew into larger ones with more bands through coalescence (**Figure 5-4 a2-c2**). Note that the orientations of the directors of each tactoid were well aligned, but they were randomly oriented with respect to each other (**Figure 5-4 b2 and c2**). Two different types of coalescence mechanisms were evidenced, which will be further discussed later. These newborn tactoids had spherical or ellipsoidal shapes, attributing to the interfacial tension between isotropic and anisotropic phases.[46] After several minutes of growth, CNCs tactoids progressively migrated to the periphery of the microdroplet (water/oil interface), driving by the phase separation induced by both the spherical confinement and Marangoni flows (**Figure 5-4 a3-c3**).[27, 47] The fusion and rearrangement of adjacent tactoids were driven by the water/oil interface tensions (**Figure 5-4 a4-c4**), generating large distinct CN domains. Interestingly, the periodic stripe patterns also bent to accommodate the spherical boundary of microdroplet (**Figure 5-4 a5-c5**). As the process progressed, the ends of flexural bands continue to

extend along with the interface until they bordered contiguous domains, triggering the onset of domain integration. Due to larger volume than tactoids, the integration process between domains tended to require a longer time, which is usually accompanied by the onset of topological defects (**Figure 5-4 a6-c6**). The vanishing of defects indicated the completion of the integration process. Spherical packing of CNCs started at the water/oil interface with the assistance of the tangential surface anchoring, and maintained the propagation toward the microdroplet centre (**Figure 5-4 a7-c7**). Newly formed spherical structures were asymmetric owing to stochastic nature in the fusion process. After approximately two hours of equilibration time, CNCs in the microdroplet exhibited uniform radial alignment (**Figure 5-4 b8**). Meanwhile, alternating bright and dark concentric rings were superimposed with a Maltese cross pattern (hedgehog point defect) that corresponded to the characteristic features of the CN phase (**Figure 5-4 a8-c8**).

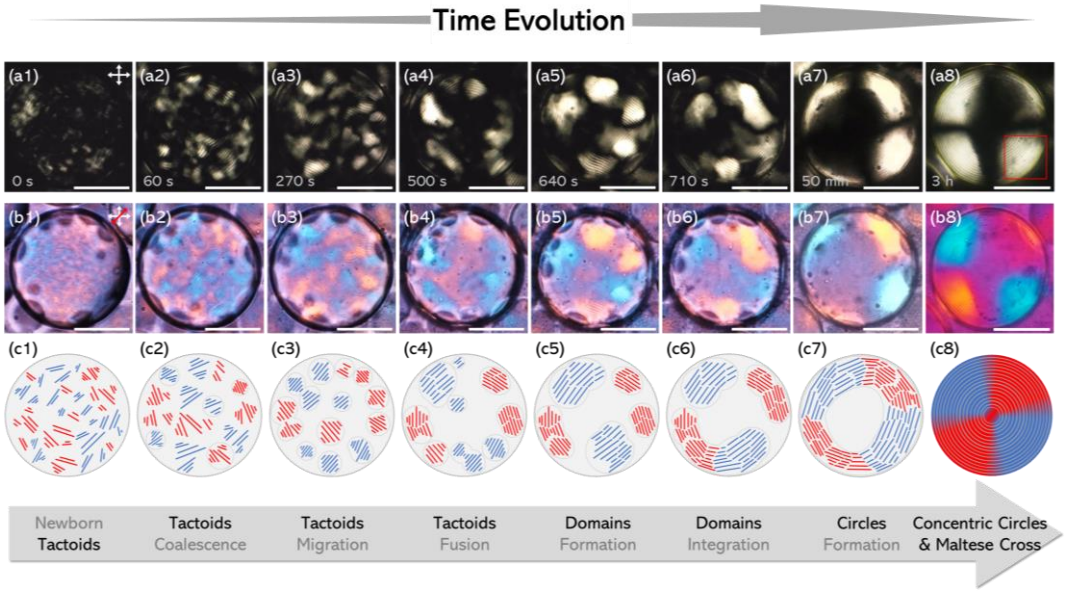

Figure 5-5. Typical POM images of time-series snapshots of TAA/$CNC_{6\%}$ microdroplet without (a1-a8) and under lambda retardation plate (b1-b8) (scale bar = 50 μm). Note that (a8) and (b8) was captured by using high magnification camera once equilibrium was reached. (c1-c8) Corresponding cartoon depiction of the microdroplet transforms from newborn tactoids to symmetrical concentric circles with Maltese cross structure.

5.7 Mechanism discussion

Distinct Maltese cross originated from the radial alignment between isoclines of the CN helix axis with respect to the polarizers.[26] Obviously, incomplete phase separation may leave an anisotropic core, exhibiting a variable pseudo-Maltese cross patterns. Since the anisotropic core equipped with a specific orientation, the central area of the pseudo-Maltese cross will alternately brighten and darken when the microdroplet remained mobile or change its orientation with respect to the polarizer. We noticed that the central region showed parallel stripes with variable widths during the brightening process (**Figure S5-4**). There were two defects at the ends of the core, which splitted one S = +1 topological charge into two S = +1/2 charges, likely contributing to minimizing the free energy of the highly frustrated liquid crystalline.[48-50] This ubiquitous phenomenon existed during the phase separation, while smaller microdroplets (further confinement) often biased towards the appearance of bipolar stripe pattern (**Figure S5-5**).[28] Maltese cross pattern with a birefringent feature covered the core of the microdroplet, which changed as the width of the lamellar core increases (**Figure S5-4**), evidencing the roles of defects.

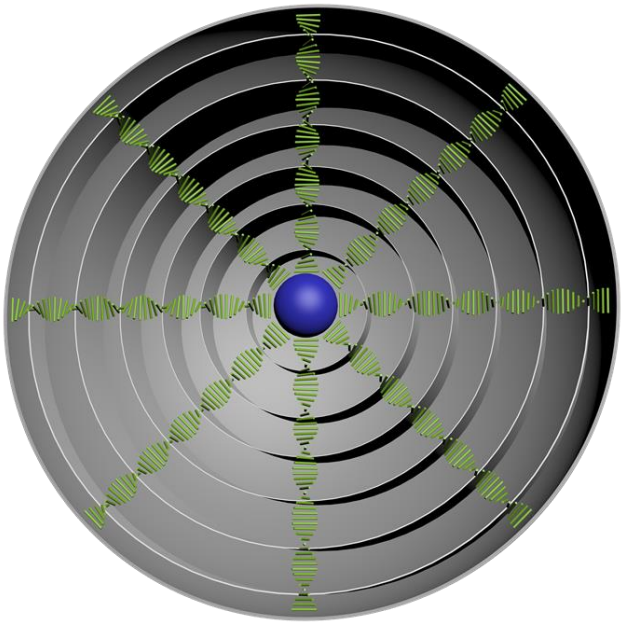

Figure 5-6. 3D model exhibits core-shell structure of TAA/$CNC_{6\%}$ microdroplet.

After adequate phase separation and a sufficient equilibrium period, the microdroplet will form a core-shell structure, that is, a CN shell with concentrically packed CNCs pseudo-layers and an isotropic core (**Figure 5-5 a8 and Figure 5-6**), where the size of core is dependent on the volume fraction of CNCs.[28, 29] Remarkably, the equilibrium state of the microdroplet has to be accompanied by a specific number of defects, such as the dislocation of spherical pseudo-layers at the microdroplet periphery (**Figure 5-7a**).[27] Such dislocation stemmed from the inconsistent relaxation progress of CNCs, leading to a local coincidence between adjacent bright spherical pseudo-layers (**Figure 5-7b**).[51]

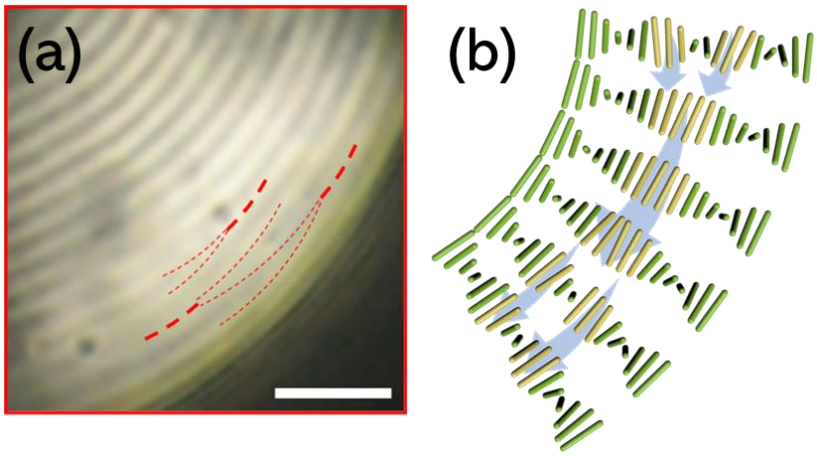

Figure 5-7. (a) POM image and (b) corresponding 3D model of a dislocation occurring in the chiral nematic layers (Figure 5-7a is derived from Figure 5-5 a8, scale bar = 10 μm).

The point of marked difference between planar and spherical geometries lies in the driving mechanism. Evaporation and sedimentation play the main roles in planar geometry, whereas in confined microdroplet, the coalescence process is driven by the phase separation induced by spherical confinement and the Marangoni flow. The conformation of tactoids stems from nucleation and rearrangement of mobile CNCs rods, while growth depends mainly on coalescence. In our observations, two different types of coalescence mechanism were depicted, namely "head-to-tail" and "side-to-side" types. The "head-to-tail" concerned two ellipsoidal-like tactoids (~ 10 μm) with quite linear helical directors. The tactoids rotated until their helical directors perfectly

matched via electrostatic attraction, resulting in a larger tactoid with multiplied periodic bands (**Figure 5-8a, Figure S5-6**). For "side-to-side" coalescence, the helical directors of two tactoids were parallel to each other, and then tilted to form a 25° angle by the attraction between the CNCs rods, allowing the insertion of the bands and eventually forming a larger tactoid with long periodic bands (**Figure 5-8b, Figure S5-7**). This coalescence type usually produced Y-shaped defects, and lasted longer than "head-to-tail" type due to the involvement of bands fusion and rearrangement. In addition, another form was sometimes observed, that is, aligned "side-to-side" coalescence (**Figure S5-8**), which tended to occur between tactoids with similar volume and the same number of bands. We do not rule out the possibility of another coalescence mechanism, such as the "head-to-side" type observed during the formation of planar films.[18] This case commonly requires high kinetics energy (e.g. during evaporation or heating) to fold the periodic bands of one tactoid and merge into another tactoid. Coalescence processes are accompanied by the appearance of defects, while they are not easy to be captured due to the small number of tactoids in early growth state and relatively short coalescence time.

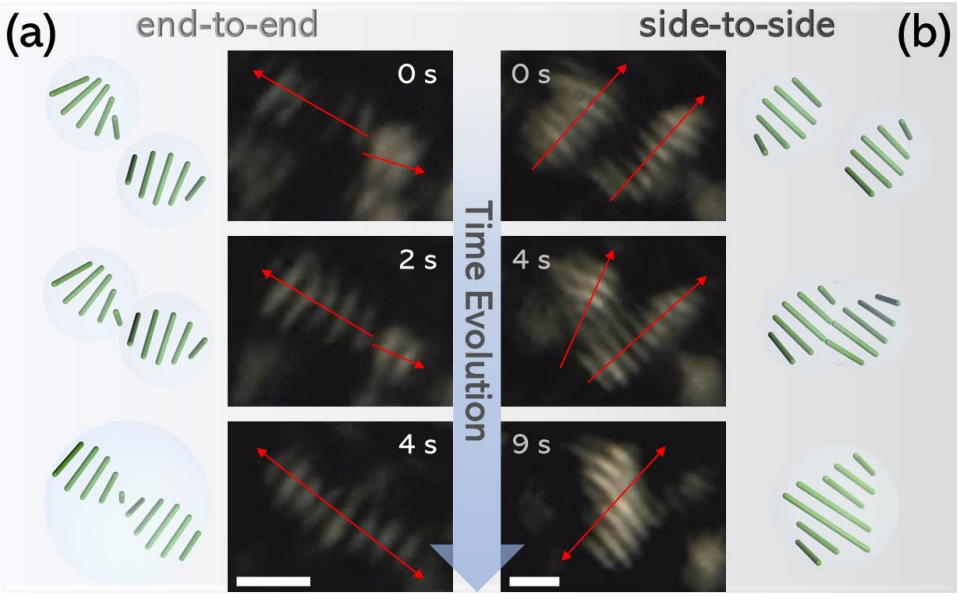

Figure 5-8. POM images and corresponding 3D models showing two different types of coalescence mechanism of tactoids: (a) head-to-tail and (b) side-to-side (scale bar = 10 μm).

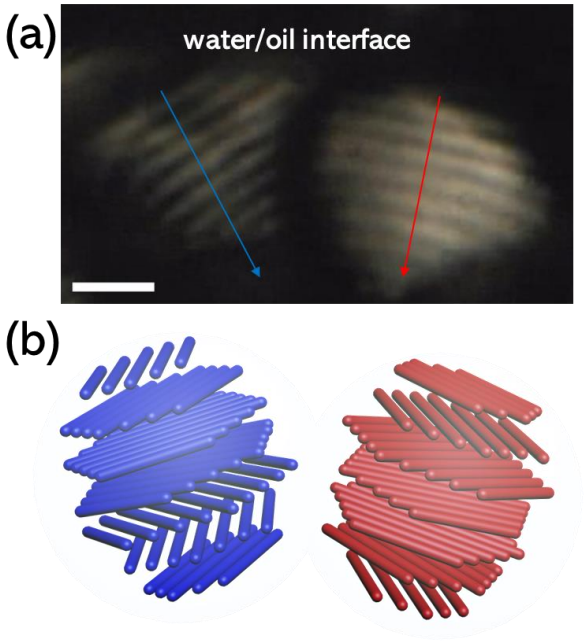

Figure 5-9. (a) POM image of tactoids anchored on the water/oil interface with their helical axes to the centre of microdroplet (scale bar = 10 μm). (b) Corresponding 3D models of anchored tactoids.

As evolution progressed, larger tactoids will gradually migrate to the periphery of the microdroplet as a result of phase separation, and will be anchored on the water/oil interface, with their helical axes pointing to the centre as well as local directors consistent with the planar anchor on microdroplet surface (**Figure 5-9**). The orientation of planar anchor was orthogonal to the helical axis and has the capability to impose spherical curvature to the periodic bands. These anchored tactoids or larger CN domains preferentially fused through the "side-to-side" pathway. Since the initial states of these domains were out of synchronization, dislocation defects were usually formed in the director field (**Figure 5-10**). Such defects, however, can be restored through the resynchronization and reorientation of the director axis due to their thermodynamic destabilization. The integration process between the two domains will last for a few minutes depending on the relaxation rate of CNCs, and will always be accompanied by obvious birefringence (**Figure 5-10 d, e**). Spherical pseudo-layers could be observed after the periphery of the microdroplet was completely packed by the CNCs domains (**Figure 5-5 a7**).

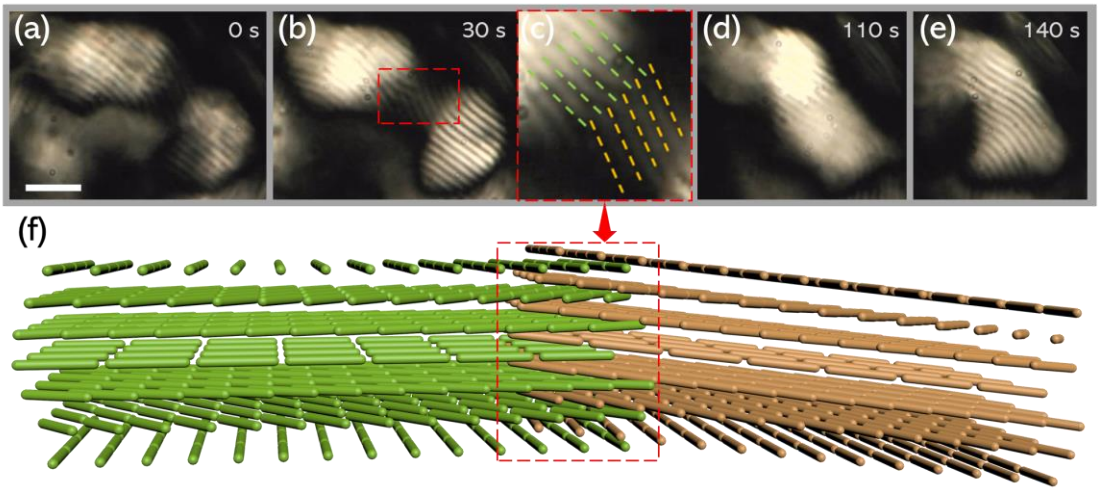

Figure 5-10. POM images revealing the dislocation and fusion occurring during the domain integration (scale bar = 20 μm) and corresponding 3D models of dislocation and fusion.

5.8 Transfer of CN structures to TiO_x/C hybrid microspheres

The concentration of CNCs plays a critical role in its self-organization process under a spherical constraint. Apart from this, an appropriate increase in temperature can promote the shortening of the evolution period. At the same time, higher temperature produced heat stress inside microdroplet, which assisted the phase separation, but also squeezed the *P* (**Figure 5-11a and Figure S5-9**). To demonstrate the feasibility of transferring such CN structures from microdroplets to solid microspheres, the TAA/$CNC_{6\%}$ microdroplets were emulsified at 60 °C for 90 min to ensure the thoroughly phase separation, and then converted into nanostructured TiO_x/C microspheres (Φ ~ 115 μm) by a hydrothermal reaction (180 °C for 18 h). Scanning electron microscopy (SEM) was used to reveal the morphology and the structure of solid TiO_x/C microspheres. The buckling and deformation of the microspheres were caused by the gradient of the pressure between TAA condensation and water extrusion during the condensation process in the hydrothermal reaction. (**Figure 5-11b**).[26, 52] Besides, there was a noticeable hole in the centre of the microsphere, pointing out a preferential localization of the TAA during the CNCs self-organization in the spherical microdroplet. The TAA was assembled in the spherical shell instead of the core. More

importantly, we observed parallel stripe patterns on the surface of microspheres (**Figure S5-10**), suggesting a potential transfer of CN structure to TiO_x/C microspheres.

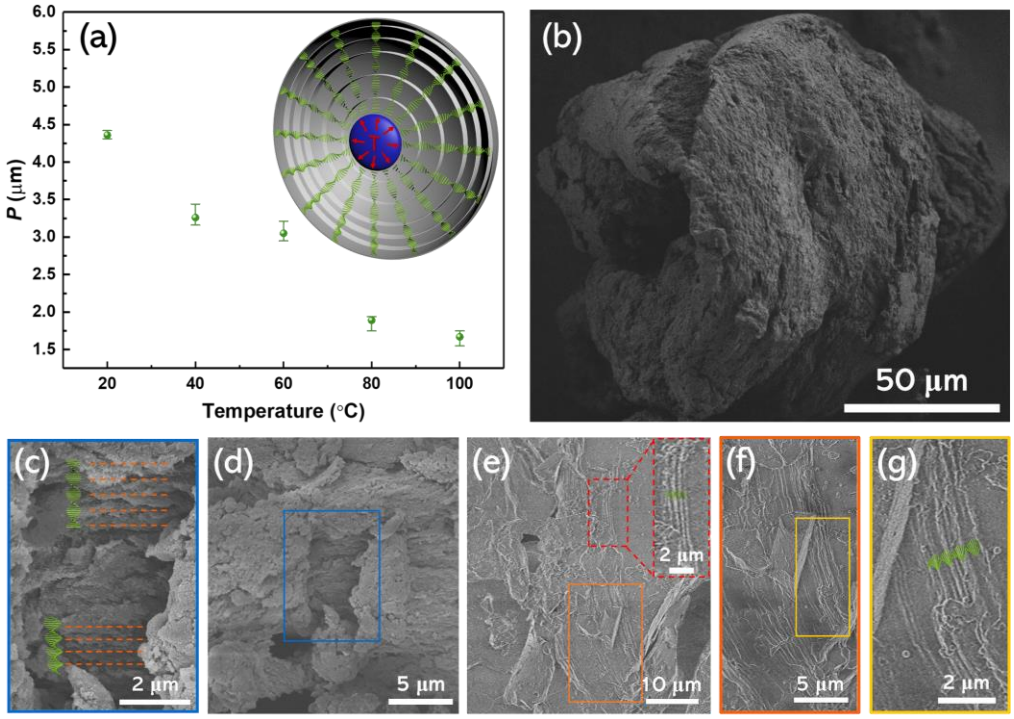

Figure 5-11. The effect of temperature on *P*. The inset is a 3D schematic diagram of *P* compressed at higher temperature. (b) SEM image of TiO_x/C microsphere with wrinkles on the surface and a hole in the centre. (c-g) Cross-section SEM images of microspheres showing CN structures with periodic lamellar bands.

To verify our hypothesis, the microspheres were cracked in liquid nitrogen after being embedded in epoxy resins, enabling the direct observation of the cross section of hybrid microspheres. The SEM images showed CN structures with periodic lamellar bands, which were captured into the TiO_x/C microsphere wall (**Figure 5-11 c-g and Figure S5-11**). This further demonstrated the successful replication of the CN structure from TAA/CNC microdroplets to hybrid TiO_x/C microspheres. The thermogravimetric analysis (TGA) was employed for identifying the titania content in TiO_x/C (**Figure S5-12**). The weight loss before 200 °C was mainly caused by the evaporation of moisture. The sharp weight decrease ranging from 200 to 420 °C corresponded to the combustion of carbon species, which implied ~ 23.5% of TiO_2 remained in TiO_x/C microspheres. Surface analysis by X-ray photoelectron spectroscopy (XPS) enabled to determine the

surface compositions of hybrid microspheres. The survey showed the presence of Ti, C and O species (**Figure S5-13**). The Ti 2p spectrum exhibited two contributions, $2p_{3/2}$ and $2p_{1/2}$ arose from spin orbit-splitting, located at respectively 459 and 464.7 eV, which is consistent with Ti^{4+} in TiO_2 (**Figure 5-12a**).[53] Likewise, the shoulder Ti $2p_{1/2}$ at 460.2 eV that corresponding to Ti^{3+} can be confirmed,[54] which could be attributed to the reduction of Ti^{4+} by carbon obtained from the dehydration of CNCs during the hydrothermal reaction. The crystalline form of TiO_x was characterized by X-ray scattering (XRS), showing the broad diffraction patterns corresponding to the nanosized TiO_2 crystallites in the anatase form (**Figure 5-12b**). Additional diffraction patterns are observed and could be attributed to sub-stoichiometric TiO_x materials, in agreement with the presence of Ti^{3+} oxidation state detected in XPS analysis. The UV-visible spectra of TiO_x/C displayed a red-shift absorption in the visible region (**Figure S5-14**), attesting to the presence of sub-stoichiometric phase in titanium dioxide. Moreover, this TiO_x/C microspheres with CN shell structures exhibited excellent photocatalytic hydrogen evolution activity (196.7 μmol g^{-1} h^{-1}) compared to commercial TiO_2-P25 (134.7 μmol g^{-1} h^{-1}) (**Figure 5-12c and Figure S5-15)**. The increase in photocatalytic activity could be attributed to the broad absorption of TiO_x/C and the light scattering induced by the CN structure of hybrid nanostructured microspheres.[55] These results provide a new perspective to obtain sub-stoichiometric titania oxides with improved light harvesting ability, showing great potential applications in photocatalysis field.

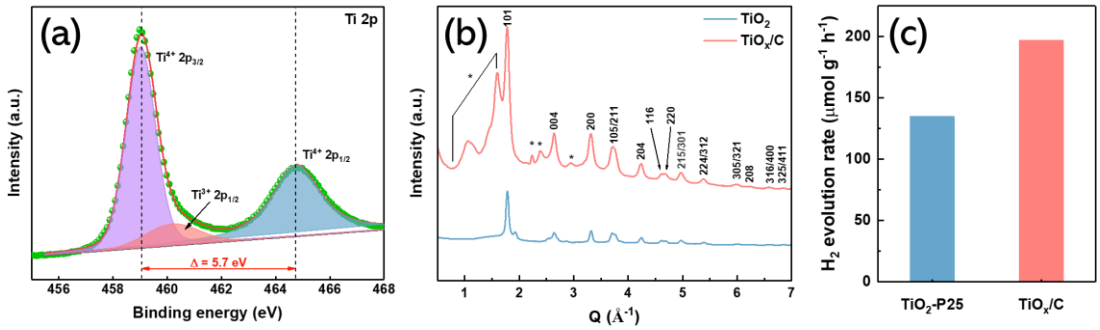

Figure 5-12. (a) XPS spectrum of Ti 2p. (b) XRS patterns of TiO_x/C microspheres. (c) Hydrogen generation constant rate of TiO_x/C microspheres and commercial TiO_2-P25.

5.9 Conclusions

In summary, we encapsulated CNCs in spherical titania-sol microdroplets using an inverse microemulsion method. We monitored the self-assembly process from seconds to hours with the aim to determine the key steps that drive the self-organization of CNCs from isotropic to chiral nematic phase in such aqueous sol. The optimization of concentration allowed to perform a real-time POM observation of the nucleation and growth of tactoids. Tactoids coalescence was the key process that guided the phase transition of mixtures from isotropic to chiral nematic phase. Two coalescence mechanisms of tactoids, "head-to-tail" and "side-to-side", were revealed during the growth process. The phase separation induced by the spherical constraint eventually leads to a microdroplet with chiral nematic shell and isotropic core. Moreover, the impact of temperature on the chiral nematic structure was investigated and a proof-of-concept of the transfer of such structure into solid TiO_x/C microspheres by hydrothermal method was demonstrated. The hybrid TiO_x/C microspheres exhibited high absorption in the visible range and promising application in photocatalytic H_2 generation. This work offers a deeper insight and substantial understanding of the assembly process of bioinspired materials in spherical geometry, and paves a promising way in the design of novel microspheres with unique chiral nematic structures, which could be widely applied in the fields of catalysis, photocatalysis and Mie scattering.

References:

1. Vanderfleet, O. M.; Cranston, E. D., Production routes to tailor the performance of

cellulose nanocrystals. *Nat. Rev. Mater.* **2021,** 6, 124-144.

2. Kose, O.; Tran, A.; Lewis, L.; Hamad, W. Y.; MacLachlan, M. J., Unwinding a spiral of cellulose nanocrystals for stimuli-responsive stretchable optics. *Nat. Commun.* **2019,** 10, (1), 1-7.

3. Giese, M.; Blusch, L. K.; Khan, M. K.; MacLachlan, M. J., Functional materials from cellulose-derived liquid-crystal templates. *Angew. Chem. Int. Ed. Engl.* **2015,** 54, (10), 2888-910.

4. Tran, A.; Boott, C. E.; MacLachlan, M. J., Understanding the Self-Assembly of Cellulose Nanocrystals-Toward Chiral Photonic Materials. *Adv. Mater.* **2020,** 32, (41), 1905876.

5. Wilts, B. D.; Whitney, H. M.; Glover, B. J.; Steiner, U.; Vignolini, S., Natural Helicoidal Structures: Morphology, Self-assembly and Optical Properties. *Materials Today: Proceedings* **2014,** 1, 177-185.

6. Wang, L.; Urbas, A. M.; Li, Q., Nature-Inspired Emerging Chiral Liquid Crystal Nanostructures: From Molecular Self-Assembly to DNA Mesophase and Nanocolloids. *Adv. Mater.* **2020,** 32, (41), e1801335.

7. Wang, C.; Li, J.; Paineau, E.; Laachachi, A.; Colbeau-Justin, C.; Remita, H.; Ghazzal, M. N., A sol–gel biotemplating route with cellulose nanocrystals to design a photocatalyst for improving hydrogen generation. *J. Mater. Chem. A* **2020,** 8, (21), 10779-10786.

8. Nguyen, T.-D.; Lizundia, E.; Niederberger, M.; Hamad, W. Y.; MacLachlan, M. J., Self-Assembly Route to TiO_2 and TiC with a Liquid Crystalline Order. *Chem. Mater.* **2019,** 31, (6), 2174-2181.

9. Xiong, R.; Luan, J.; Kang, S.; Ye, C.; Singamaneni, S.; Tsukruk, V. V., Biopolymeric photonic structures: design, fabrication, and emerging applications. *Chem. Soc. Rev.* **2020,** 49, (3), 983-1031.

10. Liu, Y.; Agthe, M.; Salajkova, M.; Gordeyeva, K.; Guccini, V.; Fall, A.; Salazar-Alvarez, G.; Schutz, C.; Bergstrom, L., Assembly of cellulose nanocrystals in a levitating drop probed by time-resolved small angle X-ray scattering. *Nanoscale* **2018,** 10, (38), 18113-18118.

11. Hiratani, T.; Hamad, W. Y.; MacLachlan, M. J., Transparent Depolarizing Organic and Inorganic Films for Optics and Sensors. *Adv. Mater.* **2017,** 29, (13).

12. Tardy, B. L.; Ago, M.; Guo, J.; Borghei, M.; Kamarainen, T.; Rojas, O. J., Optical Properties of Self-Assembled Cellulose Nanocrystals Films Suspended at Planar-Symmetrical Interfaces. *Small* **2017,** 13, (47).

13. Shopsowitz, K. E.; Qi, H.; Hamad, W. Y.; Maclachlan, M. J., Free-standing

mesoporous silica films with tunable chiral nematic structures. *Nature* **2010,** 468, (7322), 422-425.

14. Shopsowitz, K. E.; Kelly, J. A.; Hamad, W. Y.; MacLachlan, M. J., Biopolymer Templated Glass with a Twist: Controlling the Chirality, Porosity, and Photonic Properties of Silica with Cellulose Nanocrystals. *Adv. Funct. Mater.* **2014,** 24, (3), 327-338.

15. Zhao, T. H.; Parker, R. M.; Williams, C. A.; Lim, K. T. P.; Frka-Petesic, B.; Vignolini, S., Printing of Responsive Photonic Cellulose Nanocrystal Microfilm Arrays. *Adv. Funct. Mater.* **2018,** 29, (21), 1804531.

16. Wang, P. X.; MacLachlan, M. J., Liquid crystalline tactoids: ordered structure, defective coalescence and evolution in confined geometries. *Philos Trans A Math Phys Eng Sci* **2018,** 376, (2112).

17. Park, J. H.; Noh, J.; Schütz, C.; Salazar-Alvarez, G.; Scalia, G.; Bergström, L.; Lagerwall, J., Macroscopic control of helix orientation in films dried from cholesteric liquid crystalline cellulose nanocrystal suspensions. *Chemphyschem: a European journal of chemical physics and physical chemistry* **2014,** 15, (7), 1477-1484.

18. Wang, P. X.; Hamad, W. Y.; MacLachlan, M. J., Structure and transformation of tactoids in cellulose nanocrystal suspensions. *Nat. Commun.* **2016,** 7, 11515.

19. Wang, L.; Chen, D.; Gutierrez-Cuevas, K. G.; Bisoyi, H. K.; Fan, J.; Zola, R. S.; Li, G.; Urbas, A. M.; Bunning, T. J.; Weitz, D. A.; Li, Q., Optically Reconfigurable Chiral Microspheres of Self-Organized Helical Superstructures with Handedness Inversion. *Mater Horiz* **2017,** 4, (6), 1190-1195.

20. Lee, S. S.; Kim, B.; Kim, S. K.; Won, J. C.; Kim, Y. H.; Kim, S. H., Robust microfluidic encapsulation of cholesteric liquid crystals toward photonic ink capsules. *Adv. Mater.* **2015,** 27, (4), 627-33.

21. Song, D. P.; Zhao, T. H.; Guidetti, G.; Vignolini, S.; Parker, R. M., Hierarchical Photonic Pigments via the Confined Self-Assembly of Bottlebrush Block Copolymers. *ACS Nano* **2019,** 13, (2), 1764-1771.

22. Lee, S. S.; Seo, H. J.; Kim, Y. H.; Kim, S. H., Structural Color Palettes of Core-Shell Photonic Ink Capsules Containing Cholesteric Liquid Crystals. *Adv. Mater.* **2017,** 29, (23).

23. Park, S.; Lee, S. S.; Kim, S. H., Photonic Multishells Composed of Cholesteric Liquid Crystals Designed by Controlled Phase Separation in Emulsion Drops. *Adv. Mater.* **2020,** 32, (30), e2002166.

24. Noh, J.; Liang, H.-L.; Drevensek-Olenik, I.; Lagerwall, J. P. F., Tuneable multicoloured patterns from photonic cross-communication between cholesteric liquid crystal droplets. *J. Mater. Chem. C* **2014,** 2, (5), 806-810.

25. Wang, P. X.; Hamad, W. Y.; MacLachlan, M. J., Polymer and Mesoporous Silica Microspheres with Chiral Nematic Order from Cellulose Nanocrystals. *Angew. Chem. Int. Ed. Engl.* **2016,** 128, (40), 12648-12652.
26. Parker, R. M.; Frka-Petesic, B.; Guidetti, G.; Kamita, G.; Consani, G.; Abell, C.; Vignolini, S., Hierarchical Self-Assembly of Cellulose Nanocrystals in a Confined Geometry. *ACS Nano* **2016,** 10, (9), 8443-9.
27. Li, Y.; Jun-Yan Suen, J.; Prince, E.; Larin, E. M.; Klinkova, A.; Therien-Aubin, H.; Zhu, S.; Yang, B.; Helmy, A. S.; Lavrentovich, O. D.; Kumacheva, E., Colloidal cholesteric liquid crystal in spherical confinement. *Nat. Commun.* **2016,** 7, 12520.
28. Li, Y.; Nancy Khuu; Elisabeth Prince; Moien Alizadehgiashi; Elizabeth Galati; Oleg D. Lavrentovich; Kumacheva, E., Nanoparticle-laden droplets of liquid crystals: Interactive morphogenesis and dynamic assembly. *Sci. Adv.* **2019,** 5, 1-9.
29. Li, Y.; Prince, E.; Cho, S.; Salari, A.; Mosaddeghian Golestani, Y.; Lavrentovich, O. D.; Kumacheva, E., Periodic assembly of nanoparticle arrays in disclinations of cholesteric liquid crystals. *Proc. Nat. Acad. Sci.* **2017,** 114, (9), 2137-2142.
30. Araki, J.; Kuga, S., Effect of Trace Electrolyte on Liquid Crystal Type of Cellulose Microcrystals. *Langmuir* **2001,** 17, 4493-4496.
31. Dong, X. M.; Kimura, T.; Revol, J.-F.; Gray, D. G., Effects of Ionic Strength on the Isotropic−Chiral Nematic Phase Transition of Suspensions of Cellulose Crystallites. *Langmuir* **1996,** 12, 2076-2082.
32. Li, C.; Julian Evans; Nan Wang; Tingbiao Guo; He, S., pH dependence of the chirality of nematic cellulose nanocrystals. *Sci. Rep.* **2019,** 9, 1-7.
33. Bejoy Thomas; Midhun C. Raj; Athira K. B; Rubiyah M. H; Jithin Joy; Audrey Moores; Glenna L. Drisko; Sanchez, C., Nanocellulose, a Versatile Green Platform: From Biosources to Materials and Their Applications. *Chem. Rev.* **2018,** 118, (24), 11575-11625.
34. Tran, A.; Hamad, W. Y.; MacLachlan, M. J., Tactoid Annealing Improves Order in Self-Assembled Cellulose Nanocrystal Films with Chiral Nematic Structures. *Langmuir* **2018,** 34, (2), 646-652.
35. Parker, R. M.; Guidetti, G.; Williams, C. A.; Zhao, T.; Narkevicius, A.; Vignolini, S.; Frka-Petesic, B., The Self-Assembly of Cellulose Nanocrystals: Hierarchical Design of Visual Appearance. *Adv. Mater.* **2018,** 30, (19), e1704477.
36. Frka-Petesic, B.; Kelly, J. A.; Jacucci, G.; Guidetti, G.; Kamita, G.; Crossette, N. P.; Hamad, W. Y.; MacLachlan, M. J.; Vignolini, S., Retrieving the Coassembly Pathway of Composite Cellulose Nanocrystal Photonic Films from their Angular Optical Response. *Adv. Mater.* **2020,** 32, (19), e1906889.

37. Schutz, C.; Agthe, M.; Fall, A. B.; Gordeyeva, K.; Guccini, V.; Salajkova, M.; Plivelic, T. S.; Lagerwall, J. P.; Salazar-Alvarez, G.; Bergstrom, L., Rod Packing in Chiral Nematic Cellulose Nanocrystal Dispersions Studied by Small-Angle X-ray Scattering and Laser Diffraction. *Langmuir* **2015,** 31, (23), 6507-13.
38. Aline F. Miller; Donald, A. M., Imaging of Anisotropic Cellulose Suspensions Using Environmental Scanning Electron Microscopy. *Biomacromolecules* **2003,** 4, 510-517.
39. Abitbol, T.; Kam, D.; Levi-Kalisman, Y.; Gray, D. G.; Shoseyov, O., Surface Charge Influence on the Phase Separation and Viscosity of Cellulose Nanocrystals. *Langmuir* **2018,** 34, (13), 3925-3933.
40. Grelet, E.; Fraden, S., What is the origin of chirality in the cholesteric phase of virus suspensions? *Phys. Rev. Lett.* **2003,** 90, (19), 198302.
41. Straley, J. P., Theory of piezoelectricity in nematic liquid crystals, and of the cholesteric ordering. *Phys. Rev. A* **1976,** 14, (5), 1835.
42. Lagerwall, J. P. F.; Schütz, C.; Salajkova, M.; Noh, J.; Hyun Park, J.; Scalia, G.; Bergström, L., Cellulose nanocrystal-based materials: from liquid crystal self-assembly and glass formation to multifunctional thin films. *NPG Asia Materials* **2014,** 6, (1), e80-e80.
43. Yarovoy, Y.; Labes, M., Effect of chiral polymers on lyotropic liquid crystals. *J. Am. Chem. Soc.* **1997,** 119, (50), 12109-12113.
44. Wensink, H. H.; Jackson, G., Cholesteric order in systems of helical Yukawa rods. *J Phys Condens Matter* **2011,** 23, (19), 194107.
45. Onsager, L., The effects of shape on the interaction of colloidal particles. *Ann. N. Y. Acad. Sci.* **1949,** 51, (4), 627-659.
46. Chen, W.; Gray, D. G., Interfacial tension between isotropic and anisotropic phases of a suspension of rodlike particles. *Langmuir* **2002,** 18, (3), 633-637.
47. O'Keeffe, O.; Wang, P. X.; Hamad, W. Y.; MacLachlan, M. J., Boundary Geometry Effects on the Coalescence of Liquid Crystalline Tactoids and Formation of Topological Defects. *J Phys Chem Lett* **2019,** 10, (2), 278-282.
48. Xu, Y.-T.; Wang, P.-X.; MacLachlan, M. J., Self-Assembly of Two-Dimensional Colloids in Spherical Space. *J. Phys. Chem. C* **2019,** 123, (27), 17049-17055.
49. Verhoeff, A. A.; Bakelaar, I. A.; Otten, R. H.; van der Schoot, P.; Lekkerkerker, H. N., Tactoids of plate-like particles: size, shape, and director field. *Langmuir* **2011,** 27, (1), 116-25.
50. Aletta A. Verhoeff; Ronald H. J. Otten; Paul van der Schoot; Lekkerkerker, H. N. W., Shape and Director Field Deformation of Tactoids of Plate-Like Colloids in a Magnetic Field. *J. Phys. Chem. B* **2009,** 113, 3704–3708.

51. Khadem, S. A.; Bagnani, M.; Mezzenga, R.; Rey, A. D., Relaxation dynamics in bio-colloidal cholesteric liquid crystals confined to cylindrical geometry. *Nat. Commun.* **2020,** 11, (1), 4616.
52. Cerda, E.; Mahadevan, L., Geometry and physics of wrinkling. *Phys. Rev. Lett.* **2003,** 90, (7), 074302.
53. Ghazzal, M. N.; Kebaili, H.; Joseph, M.; Debecker, D. P.; Eloy, P.; De Coninck, J.; Gaigneaux, E. M., Photocatalytic degradation of Rhodamine 6G on mesoporous titania films: Combined effect of texture and dye aggregation forms. *Appl. Catal. B* **2012,** 115-116, 276-284.
54. Bharti, B.; Kumar, S.; Lee, H. N.; Kumar, R., Formation of oxygen vacancies and Ti(3+) state in TiO2 thin film and enhanced optical properties by air plasma treatment. *Sci Rep* **2016,** 6, 32355.
55. Gesesse, G. D.; Li, C.; Paineau, E.; Habibi, Y.; Remita, H.; Colbeau-Justin, C.; Ghazzal, M. N., Enhanced Photogenerated Charge Carriers and Photocatalytic Activity of Biotemplated Mesoporous TiO_2 Films with a Chiral Nematic Structure. *Chem. Mater.* **2019,** 31, (13), 4851-4863.